Origin of the distinct thermoelectric transport properties of chalcopyrite $ABTe_2$ (A=Cu, Ag; B=Ga, In)

Yu Cao[1], Xianli Su[1*], Fanchen Meng[2], Trevor P. Bailey[3], Jinggeng Zhao[4], Hongyao Xie[1], Jian He[2*], Ctirad Uher[3], Xinfeng Tang[1*]

Dr. Y. Cao, Prof. X. Su, Dr. H. Xie, Prof. X. Tang

State Key Laboratory of Advanced Technology for Materials Synthesis and Processing

Wuhan University of Technology

Wuhan 430070, China

E-mail: suxianli@whut.edu.cn, tangxf@whut.edu.cn

Dr. F. Meng, Prof. J. He

Department of physics and astronomy

Clemson University

Clemson 29634, USA

E-mail: jianhe@g.clemson.edu

Dr. T. P. Bailey, Prof. C. Uher

Department of Physics

University of Michigan

Ann Arbor, MI 48109, USA

Prof. J. Zhao

School of Physics

Author Manuscript

This is the author manuscript accepted for publication and has undergone full peer review but has not been through the copyediting, typesetting, pagination and proofreading process, which may lead to differences between this version and the Version of Record. Please cite this article as doi: 10.1002/adfm.202005861.

This article is protected by copyright. All rights reserved.

Harbin Institute of Technology

Harbin 150080, China

Keywords: chalcopyrites, deep levels, boson peak, phonon scattering, thermoelectric

Abstract: Despite the same crystal structure and homologous constituent elements, the chalcopyrite compounds $ABTe_2$ (A=Cu, Ag; B=Ga, In) exhibit distinct electronic and thermal transport properties. In this work, we aim to understand the origin of such discrepancy by means of experiments and theoretical calculations. The results of Hall coefficient measurements, absorption spectroscopy, and electronic transport studies suggest the deep-level in-gap states induced by the native A-site vacancies play a key role in the observed intrinsic semiconductor to degenerate semiconductor transition and are the origins of the distinct electrical conductivity among the four $ABTe_2$ compounds. Besides, the cryogenic heat capacity measurements and calculated phonon dispersion relations show that the acoustic and low-frequency optical modes of $AgGaTe_2$ and $AgInTe_2$ are governed by the vibrations of Ag-Te clusters while the counterparts of $CuGaTe_2$ and $CuInTe_2$ compounds are dominated by the vibrations of Te atoms, and the coupling between the acoustic and low-frequency optical modes is notably different among the $ABTe_2$ compounds. Specifically, lower avoided-crossing frequencies, lower sound velocity together with stronger Umklapp process yielded lower thermal conductivities of $AgGaTe_2$ and $AgInTe_2$ than $CuGaTe_2$ and $CuInTe_2$. The work provides new insights into the understanding and improvement of

Author Manuscript

This article is protected by copyright. All rights reserved.

electronic and thermal transport properties towards higher thermoelectric performance of chalcopyrite compounds.

Author Manuscript

This article is protected by copyright. All rights reserved.

1. Introduction

In the past couple of decades, the increasing energy and environmental crises have made the development of environment-friendly renewable energy materials and related energy conversion technologies a research focus worldwide.[1–4] Thermoelectric materials that can accomplish efficient conversion between heat and electricity have attracted much attention.[5–9] The conversion efficiency of thermoelectric material is evaluated by its dimensionless figure of merit $ZT = \frac{\sigma S^2 T}{\kappa}$, where σ, S, κ and T are the electrical conductivity, the Seebeck coefficient, the total thermal conductivity, and the absolute temperature, respectively. Towards an efficient thermoelectric material, both its electrical conductivity and Seebeck coefficient should be as large as possible, while its ability to conduct heat should be minimized.[10–12] Though there is no known theoretical limit for maximum *ZT*, the strong and adverse coupling among the σ, S, κ makes the improvement of *ZT* a challenge in practice. Numerous investigations document[13–17] that among the effective strategies to boost the thermoelectric performance are appropriate levels of doping, formation of solid solutions, and nanostructuring, including fabrication of nanocomposite materials. Through the above strategies, high thermoelectric performance has been achieved in PbTe-based materials,[18–20] BiSbTe alloys,[21–23] filled skutterudites,[24–26] SnTe-based materials[27–29] and BiCuSeO[30–32] over a wide temperature range. Nevertheless, there is always an urgent need for developing new thermoelectric materials.

In recent years, compounds with the diamond-type structure, such as $AgGaTe_2$,[33,34] Cu_2SnX_3(X=Se, S),[35–38] and $CuFeS_2$,[39–41] have drawn lots of interests in the field of

This article is protected by copyright. All rights reserved.

Author Manuscript

thermoelectrics due to their highly tunable crystal structures and electronic band structures,[42,43] leading to highly tunable physical properties. For example, a maximum *ZT* value of 0.5 was obtained at 800 K in pristine $CuGaTe_2$[44] taking advantage of its excellent electrical properties. In addition, with proper doping and forming solid solutions, a higher *ZT* value of 1.3 at 865 K was achieved in $Cu(Ga_{0.75}In_{0.25})_{0.99}Zn_{0.01}Te_2$.[45] Hence, $ABTe_2$ (A=Cu, Ag; B=Ga, In) compounds hold great promise as potential high-performance thermoelectric materials.

Of special interest is that despite the same crystal structure and similar constituent elements, the $ABTe_2$ chalcopyrites exhibit very different electronic and thermal transport properties.[33,46–48] Concerning the electrical conductivity at room temperature, $CuGaTe_2$ and $CuInTe_2$,[46,47,49] possess electrical conductivities of about 2.1×10^3 S/m and 4.1×10^3 S/m, respectively, while much lower electrical conductivities of around 0.35 S/m and 4.8 S/m are obtained for $AgGaTe_2$ and $AgInTe_2$,[50,51] respectively. For the thermal conductivity at 300 K, $AgGaTe_2$ and $AgInTe_2$[50,51] exhibit thermal conductivities of 1.77 $Wm^{-1}K^{-1}$ and 0.92 $Wm^{-1}K^{-1}$, respectively, whereas the thermal conductivities are 7.40 $Wm^{-1}K^{-1}$ and 6.60 $Wm^{-1}K^{-1}$ for $CuGaTe_2$ and $CuInTe_2$,[46,47] respectively. In light of the isoelectronic substitution between Ag and Cu along with Ga and In, the origin of such discrepancies in both electrical and thermal transport properties is unknown and worth investigation. This is the primary motivation for this work.

Author Manuscript

This article is protected by copyright. All rights reserved.

Another interesting feature in the pristine $ABTe_2$ chalcopyrites is the intrinsic semiconductor to degenerate semiconductor transition at high temperatures. As known, traditional high-performance thermoelectric materials, such as Bi_2Te_3-based and PbTe-based compounds, etc., are heavily-doped semiconductors.[52–54] Due to the onset of intrinsic excitations, the electrical conductivity and the bipolar thermal conductivity of these materials rises dramatically with increasing temperature, and the Seebeck coefficient decreases, degrading the thermoelectric performance. In contrast, the electronic transport properties of the $ABTe_2$ compounds are less affected by the detrimental bipolar effect due to their much larger band gaps on the order of 1 eV.[34,55–59] More interestingly, we in this work found that the pristine $ABTe_2$ (A=Cu, Ag; B=Ga, In) chalcopyrites exhibit intrinsic semiconductor to degenerate semiconductor transitions between 700 K to 800 K, the origin of which is found to be related to the deep level in-gap states induced by native A-site vacancies.

We also study the profound effects of constituent elements on the chemical bond length, angle, and strength, which in turn affect the phonon dispersion relation and thermal conductivity. Specifically, the analyses of low temperature heat capacity and calculated phonon dispersion relations reveal the distinction between the dominance of Ag-Te cluster vibrations in low-frequency phonon spectra of $AgGaTe_2$ and $AgInTe_2$ as opposed to the dominance of Te vibrations in the counterparts of $CuGaTe_2$ and $CuInTe_2$. The extent of the coupling between low-frequency optical phonon and acoustic phonon is distinct, $CuGaTe_2$ and $CuInTe_2$ possess higher avoided-crossing frequencies and sound velocity than $AgGaTe_2$ and $AgInTe_2$. In addition, the weak chemical bonds in $AgGaTe_2$ and $AgInTe_2$ result in a

This article is protected by copyright. All rights reserved.

Author Manuscript

lower sound velocity that in turn enhances the Umklapp process, yielding lower thermal conductivities in $AgGaTe_2$ and $AgInTe_2$.

2. Results and Discussion

2.1. Phase Composition and Micro Structure

Figure 1a shows powder X-ray diffraction (XRD) patterns at room temperature. All four samples are single phase with a diamond-type structure and the space group of *I*42*d*. Rietveld refinements were employed to derive the lattice constants, bond lengths, and bond angles, and the results are shown in **Figure 2** and **Table 1**. For conciseness, we choose and discuss $AgGaTe_2$ as an example. The crystal structure of the $AgGaTe_2$ compound is composed of three types of building blocks ($AgTe_4$, $GaTe_4$, and Ag_2Ga_2Te), of which corner-shared $AgTe_4$ and $GaTe_4$ tetrahedrons are inter-connected into the three-dimensional diamond-type crystal structure. Two adjacent Ag atoms and two adjacent Ga atoms form a tetrahedron, at the center of which resides a Te atom. The bond length of the Ag-Te bond is 2.76 Å, longer than that of the Ga-Te bond of 2.62 Å. The other three compounds possess a similar structure with somewhat different bond lengths and angles. The lattice parameter along the *a*-axis increases from 6.02 Å to 6.45 Å in order from $CuGaTe_2$ to $CuInTe_2$, to $AgGaTe_2$, and finally to $AgInTe_2$. Meanwhile, the lattice parameter along *c*-axis increases from 11.94 Å to 12.65 Å in the order from $CuGaTe_2$ to $AgGaTe_2$ to $CuInTe_2$ and finally to $AgInTe_2$. The lattice constant difference is ascribed to the distinct chemical bond lengths and

This article is protected by copyright. All rights reserved.

Author Manuscript

angles in the four chalcopyrite compounds, which in turn govern their phonon dispersion relations. Specifically, the Cu-Te bond lengths of 2.58 Å in $CuGaTe_2$ and 2.59 Å in $CuInTe_2$ are shorter than the Ag-Te bond lengths of 2.76 Å in $AgGaTe_2$ and 2.78 Å in $AgInTe_2$. The Cu-Te-Ga bond angle is 109.22° and the Cu-Te-In bond angle is 109.26°, which are closer to the regular tetrahedral angle of 109.5° and smaller than the Ag-Te-Ga bond angle of 112.20° and the Ag-Te-In bond angle of 110.56°.

Concerning the micro-morphology, the fracture surfaces are found to have practically the same micro-morphology for the four samples. As shown in **Figure 3**, the freshly fractured surface of the $CuGaTe_2$ sample exhibits brittle fracture with trans-granular features. The staircase-type cleavage plane is observed with the average grain size of about 20 μm. Close similarities in the microstructure of the four compounds, therefore, rule out the microstructure as the origin of their distinct transport behaviors.

2.2. Electronic Transport Characterization

2.2.1. Electronic Transport Properties

Figure 4 shows the temperature dependences of the electrical conductivity, Seebeck coefficient, and power factor of the four compounds. As depicted in **Figure 4a**, unlike the typical electrical conductivity behavior of traditional thermoelectric materials with shallow-level in-gap impurity states, all four compounds undergo an unusual intrinsic

Author Manuscript

This article is protected by copyright. All rights reserved.

semiconductor to degenerate semiconductor transition (crossover). From 300 K to around 750 K, all four compounds behave like semiconductors as their electrical conductivities increase with increasing temperature. However, upon a further increase in temperature, the electrical conductivity levels off and then decreases, the transition is more salient in $AgGaTe_2$ and $AgInTe_2$. The transitions in $AgGaTe_2$ and $AgInTe_2$ take place at temperatures about 100 K lower than in $CuGaTe_2$ and $CuInTe_2$, and the electrical conductivities of the former two compounds are about two orders of magnitude lower than the latter two compounds (e.g., only 1.76×10^2 S/m for $AgInTe_2$ at 727 K compared to 1.49×10^4 S/m for $CuGaTe_2$ at the same temperature). **Figure 4b** shows that all samples exhibit positive Seebeck coefficients over the entire temperature range, indicating that holes are the majority charge carrier. The Seebeck coefficient generally exhibits a temperature dependence opposite to that of electrical conductivities, i.e., the magnitude of the Seebeck coefficient decreases from 300 K, reaches its minimum value between 700 K and 800 K, levels off, and then increases at higher temperatures. Due to the excellent electrical conductivity, the $CuGaTe_2$ and $CuInTe_2$ compounds have larger power factors than the $AgGaTe_2$ and $AgInTe_2$ compounds (**Figure 4c**). The largest power factor of 1.40 mW/mK^2 at 794 K is obtained for the $CuGaTe_2$ compounds, the value is comparable to the traditional thermoelectric materials, such as PbTe[60] and $AgSbTe_2$.[61–63]

2.2.2. Underlying Mechanisms for Electronic Transport

Author Manuscript

This article is protected by copyright. All rights reserved.

The electronic transport properties of materials are closely related to their electronic band structure and scattering mechanism. The results of temperature variable high-resolution synchrotron powder diffraction measurements[33] indicated that there are no phase transitions from 300 K to 850 K. Therefore, the intrinsic semiconductor to degenerate semiconductor transitions observed in the $ABTe_2$ (A=Cu, Ag; B=Ga, In) compounds may be attributed to the change of charge carrier concentration and/or the change of dominant scattering mechanism. Inferring from the temperature dependent carrier concentration shown in **Figure 5c,** the carrier concentration quick increases above 600 K. In light of the relatively large value of band gap (**Figure 5b**), it suggests the presence of deep-level in-gap impurity states, the thermal excitation of these states populates the valence band with holes and drives the material from a non-degenerate semiconductor to a degenerate semiconductor. The argument is consistent with the temperature variations of electrical conductivity and Seebeck coefficient (**cf. Figure 4a and Figure 4b**).

To probe the presence of deep-level in-gap impurity states, the absorption coefficient at different wavelengths was measured on the four samples (**Figure 5a** and **Figure 5b**). The measured optical bandgaps of $AgGaTe_2$, $AgInTe_2$, $CuGaTe_2$ and $CuInTe_2$ are respectively 1.06 eV, 0.87 eV, 1.18 eV and 0.92 eV, agreeing with the literature data.[34,55,56] Apart from the absorption corresponding to the valence band edge, an additional peak is observed in the optical spectra. The energy value of this extra peak is around 0.43 eV for $AgGaTe_2$ and $AgInTe_2$ samples and 0.63 eV for $CuGaTe_2$ and $CuInTe_2$. Hence, the extra peak, in conjunction with the aforementioned temperature variation of carrier concentration (cf.

This article is protected by copyright. All rights reserved.

Author Manuscript

Figure 5c), indicates the presence of deep-level in-gap impurity states. Assuming the temperature range of 300 K to 700 K is within the freeze-out range, the carrier concentration of $CuGaTe_2$ and $CuInTe_2$ as a function of temperature can be expressed as:[64]

$$p = \left(\frac{N_A N_V}{2}\right)^{1/2} exp\left(-\frac{\Delta E_A}{2k_B T}\right) \propto T^{3/4} exp\left(-\frac{\Delta E_A}{2k_B T}\right). \quad (1)$$

Here, N_A is the concentration of acceptor impurities, N_V is the effective density of states in the valence band proportional to $T^{3/2}$, ΔE_A is the ionization energy given as $\Delta E_A = E_A - E_V$, where E_A is the acceptor level. The ionization energy of impurity level can be obtained from the slope of $ln(pT^{-3/4})$ versus $1000/T$ curve (cf. the inset of **Figure 5c**). The derived ionization energies of impurity band in $CuGaTe_2$ and $CuInTe_2$ are 0.52 and 0.61 eV, respectively. These values are fairly close to the values derived from the spectroscopy study discussed above. In addition, the fitting also suggests the presence of shallow impurity levels with the ionization energy of 0.11 and 0.13 eV and a small number of states in $CuGaTe_2$ and $CuInTe_2$.

Based on the data of absorption spectra and Hall coefficient, we draw a schematic electronic band diagram that displays the valence band edge in relation to the conduction band edge, the Fermi level, and the impurity levels in **Figure 6**. There are some common features among these four compounds. First, the Fermi levels of all compounds are located within the bandgap at room temperature. This argument is in accord with that the compounds exhibit semiconducting characteristics in the temperature range from 300 K to around 750 K. The work functions of the four samples are consistent with the values reported in the

Author Manuscript

This article is protected by copyright. All rights reserved.

literature,[65] all falling in the range from 5.3 eV to 5.6 eV. On the other hand, there are some notable differences among these four compounds. For example, the energies of acceptor impurity levels in $AgGaTe_2$ and $AgInTe_2$ are 0.4 eV above the valence band edge, while they are 0.6 eV above the valence band edge in $CuGaTe_2$ and $CuInTe_2$. The lower ionization energies of impurity levels in $AgGaTe_2$ and $AgInTe_2$ thus explain their lower intrinsic semiconductor to degenerate semiconductor transition temperatures of around 700 K compared with those values of about 800 K in $CuGaTe_2$ and $CuInTe_2$.

The presence of monovalent element vacancies in these compounds is the origin of deep-level states. Shen *et al*.[44] calculated the formation energies of several kinds of defects in $AgGaTe_2$ and $CuGaTe_2$. They found the formation energies of Cu vacancy in $CuGaTe_2$ and Ag vacancy in $AgGaTe_2$ with the values of 0.27 eV and 0.62 eV, respectively, are much smaller than the formation energies of other possible defects. Ag or Cu vacancies act as acceptors, consistent with the *p*-type conduction. In the pseudo-binary phase diagram of A_2Te-B_2Te_3,[66,67] $ABTe_2$ compounds are not line phases, and a trace amount of compositional deviation from the nominal content would result in the Ag and Cu vacancies. Hence, the Ag and Cu vacancies induced deep levels govern the distinct semiconductor behavior in electronic transport characteristics of the four compounds from 300 K to around 750 K.

2.3. Thermal Transport Characterization

Author Manuscript

This article is protected by copyright. All rights reserved.

2.3.1. Thermal Transport Properties

The temperature dependences of the total thermal conductivity, carrier thermal conductivity, lattice thermal conductivity, and *ZT* values are presented in **Figure 7**. As discussed in the electronic transport properties section, the electrical conductivities of the four compounds exhibit intrinsic semiconductor to degenerate semiconductor transitions. The total thermal conductivities of the four compounds decrease with increasing temperature in the temperature range studied. The carrier thermal conductivity (**Figure 7b**) can be estimated from the measured electrical conductivity σ by employing the Wiedemann-Franz law,[68,69] $\kappa_e = L\sigma T$. In this formula, L represents the Lorenz number that can be calculated from Eq. 2 with the assumption that the electronic band structure of the materials approximately satisfies a single parabolic band model:

$$L = \left(\frac{k_B}{e}\right)^2 \left\{\frac{(r+7/2)F_{r+5/2}(\eta)}{(r+3/2)F_{r+1/2}(\eta)} - \left[\frac{(r+5/2)F_{r+3/2}(\eta)}{(r+3/2)F_{r+1/2}(\eta)}\right]^2\right\}. \quad (2)$$

Here, η is the reduced Fermi energy calculated from the measured Seebeck coefficient α via combining Eq. 3 and Eq. 4:

$$\alpha = \pm\frac{k_B}{e}\left[\frac{(r+5/2)F_{r+3/2}(\eta)}{(r+3/2)F_{r+1/2}(\eta)} - \eta\right]. \quad (3)$$

$$F_n(\eta) = \int_0^\infty \frac{\chi^n}{1+e^{\chi-\eta}}\,d\chi. \quad (4)$$

In Eqs. 2 and 3, k_B stands for the Boltzmann constant, e represents the electron charge, and r is the scattering factor, taken here equal to –1/2 for acoustic phonon scattering. The

This article is protected by copyright. All rights reserved.

Author Manuscript

contribution of the charge carriers to the overall thermal conductivity is relatively small because of rather poor electrical conductivities of the compounds. The lattice thermal conductivity thus dominates the total thermal conductivity. As illustrated in the inset of **Figure 7c**, the lattice thermal conductivity decreases dramatically with increasing temperature, the inverse temperature dependence is the signature of Umklapp process. The lattice thermal conductivities of $CuGaTe_2$ and $CuInTe_2$ compounds are significantly larger than those of $AgGaTe_2$ and $AgInTe_2$, particularly at low temperatures. As shown in **Figure 7a**, the total thermal conductivity of $CuInTe_2$ is 5.9 $Wm^{-1}K^{-1}$ at 300 K, while that of $AgInTe_2$ is 1.4 $Wm^{-1}K^{-1}$ at 300 K. The Cu-containing compounds show a much sharper decrease in their thermal conductivity than the Ag-containing compounds, consistent with the larger average sound velocity, higher Grüeneissen parameters γ calculated from the sound velocity measured *via* the pulse-echo method (**Table 3**) and the larger coupling between acoustic phonons and low-frequency optic phonons of the Cu-containing compounds. At 873 K, $CuInTe_2$ and $AgInTe_2$ reach values of 0.98 $Wm^{-1}K^{-1}$ and 0.23 $Wm^{-1}K^{-1}$, respectively. With both electrical and thermal properties considered, despite rather high thermal conductivities of $CuGaTe_2$ and $CuInTe_2$ compounds, their *ZT* values reach above 0.9 at 873 K. In contrast, the performance of the $AgGaTe_2$ and $AgInTe_2$ compounds is inferior, the maximum *ZT* value of $AgGaTe_2$ not exceeding 0.5 and that of $AgInTe_2$ reaching merely 0.2 (cf. **Figure 7d**).

2.3.2. Underlying Mechanisms for Thermal Transport

Author Manuscript

This article is protected by copyright. All rights reserved.

To give more insights into the differences in thermal transport properties among the four compounds, we measured the low-temperature heat capacity from 2 K to 300 K, the data are displayed in **Figure 8a**. As the temperature increase, more phonon modes are excited, the heat capacity increases steadily and reaches the Dulong-Petit limiting value of 99.8 $Jmol^{-1}K^{-1}$ for $ABTe_2$ compounds at 300 K. In the temperature range between 2 K and 16 K, the experimental heat capacity can be fitted well using a Debye-Einstein model (Eq. 5):

$$\frac{C_{\mathrm{p}}}{T^3} = \frac{\gamma}{T^2} + b + \sum_{i=1}^{n} \frac{A_i(\theta_{\mathrm{Ei}})^2}{T^5} \cdot \frac{e^{\theta_{\mathrm{Ei}}/T}}{(e^{\theta_{\mathrm{Ei}}/T} - 1)^2}. \quad (5)$$

The first term in Eq. 5 represents the contribution from electrons with the coefficient γ given by Eq. 6:

$$\gamma = \frac{\pi^2}{3} k_{\mathrm{B}}^2 N(E_{\mathrm{F}}) = 1.36 \times 10^{-4} \times V_{mol}^{\frac{2}{3}} n_{\gamma}^{\frac{1}{3}} \frac{m^*}{m_0}. \quad (6)$$

Here, V_{mol} is the molar volume, n_{γ} is the number of electrons, m^* is the density of states effective mass, and m_0 is the bare electron mass. The γ term can be ignored because the four compounds are practically insulating at low temperatures. The second term in Eq. 5 stands for the Debye phonon modes with b given by Eq. 7:

$$b = \frac{12C\pi^4 N_{\mathrm{A}} k_{\mathrm{B}}}{5\theta_D^3}. \quad (7)$$

The parameter C follows from the formula $C = 1 - \sum_i A_{\mathrm{i}}/3NR$, where R is the gas constant and N is the number of atoms per unit cell. The third term in Eq. 5 is the contribution from the localized Einstein oscillator modes, and n represents the number of localized Einstein

This article is protected by copyright. All rights reserved.

Author Manuscript

oscillator modes. The amount and the Einstein temperature of the ith Einstein oscillator mode are represented by A_i and E_i, respectively. As shown in **Figure 8b**, the heat capacity data can be well fitted by two Einstein oscillators in the Debye host. The respective fitting parameters, including the Debye temperature and the two Einstein temperatures, are summarized in **Table 2**.

As displayed in **Figure 8b**, the C_p/T^3 vs. T curves for the four compounds substantially deviate from the conventional Debye model $C_p \propto T^3$, exhibiting prominent maxima that we refer to as Boson peaks. We observe an interesting correlation: the larger the thermal conductivity, the lower and broader the boson peak.

In practice, the low-temperature heat capacity is typically described by the Debye model in the long-wavelength limit approximation. However, in systems possessing intrinsically low lattice thermal conductivity, such as amorphous structures, glasses, and highly disordered crystal structures, due to the presence of low-frequency oscillator modes, a Boson peak is often observed in the plot of C_p/T^3 vs. T The physical origin of the Boson peak remains a topic without consensus.[70–80] Some[70] argued that the Boson peak arises from the disorder-induced broadening of the transverse acoustic phonons or the Ioffe-Regel crossover at large acoustic wavelengths, also referred to as the van Hove singularity. Others[9,73–75,78] attribute the Boson peak to the strong coupling between acoustic phonons and low-frequency optic phonons, which has been observed in $BaAg_2SnSe_4$,[9] Cd_2ReO_7,[78] and $CuFeS_2$.[81] For instance, in $BaAg_2SnSe_4$,[9] the vibrations of the Ag-Se cluster act as two Einstein oscillators

This article is protected by copyright. All rights reserved.

Author Manuscript

in the Debye host. This leads to an ultralow thermal conductivity in $BaAg_2SnSe_4$. Our experimental results obtained on the four $ABTe_2$ compounds suggest the idea that the Boson peak arises as a consequence of strong coupling between acoustic phonons and low-frequency optic phonons. Such strong coupling produces a low avoided-crossing frequency for Debye modes in the first Brillouin zone and leads to a low sound velocity. The stronger the coupling, the lower the avoided-crossing frequency and thus the lower thermal conductivity.

To support these arguments, we computed the phonon dispersion relations, phonon density of states, and projected (element-specific) phonon density of states using density functional perturbation theory calculations. As shown in **Figure 9**, strong coupling between acoustic phonons and low-frequency optic phonons is, indeed, observed in the phonon dispersion relations for all four compounds. However, the phonon dispersion relations within the first Brillouin zone differ from each other in several aspects. First, as exhibited in **Figure 9**, the avoided-crossing frequencies of acoustic phonons for the $AgGaTe_2$ and $AgInTe_2$ compounds are lower than those for $CuGaTe_2$ and $CuInTe_2$ compounds along the same direction. In addition, the Ga-containing compounds possess higher avoided-crossing frequencies than the In-containing compounds. For example, the avoided-crossing frequencies for the longitudinal acoustical phonons of $AgGaTe_2$, $AgInTe_2$, $CuGaTe_2$, and $CuInTe_2$ are 38 cm^{-1}, 35 cm^{-1}, 53 cm^{-1}, and 46 cm^{-1}, respectively, which are consistent with the corresponding Einstein temperatures obtained from the low-temperature heat capacity fitting. Such significantly different avoided-crossing frequencies may help explain the

This article is protected by copyright. All rights reserved.

Author Manuscript

distinct thermal conductivities of the four compounds. Specifically, higher avoided-crossing frequencies and sound velocities for the $CuGaTe_2$ and $CuInTe_2$ compounds indicate the smaller phonon densities of states below 40 cm^{-1}, which contributes to their lower and broader boson peak observed in the low-temperature heat capacity. From the smaller slopes in acoustic phonon dispersions of the $AgGaTe_2$ and $AgInTe_2$ compounds compared to those of the $CuGaTe_2$ and $CuInTe_2$ compounds, it follows that the former compounds possess smaller group velocities than the latter compounds. In general, lower group velocities are viewed as a reflection of the lower lattice thermal conductivity and larger anharmonicity in the lattice vibrations.[9,74,82] Specifically, for one transverse acoustic phonons along the Γ-X direction, the slope for $AgInTe_2$ is 1189 ms^{-1}, while the slope for $CuGaTe_2$ is 1765 ms^{-1}. The slopes of the phonon spectra of the four compounds are consistent with the values of the sound velocity measured *v*ia the pulse-echo method (**Table 3**). The shear sound velocity is 1378 ms^{-1} for $AgGaTe_2$, lower than that for the $CuGaTe_2$ compound of 2081 ms^{-1}. The difference in the average sound velocity partially accounts for the thermal conductivity difference among the four compounds. We conclude that the strong coupling between acoustic phonons and low-frequency optic phonon modes gives rise to a low avoided-crossing frequency of acoustic phonons, which suppresses the sound velocity. The stronger coupling, the lower avoided-crossing frequency of acoustic phonons, and their lower sound velocity result in a lower lattice thermal conductivity.

The calculated projected phonon densities of states for the four compounds reveal contributions of each atom to the phonon spectrum, and specifically to the heat-carrying

This article is protected by copyright. All rights reserved.

Author Manuscript

acoustic modes together with the low-frequency optic phonons. Notably, the vibrations of Ag and Te atoms dominate the acoustic phonon modes in the $AgGaTe_2$ and $AgInTe_2$ compounds, while vibrations of Te atoms are the main contribution in the $CuGaTe_2$ and $CuInTe_2$ compounds. Regarding the low-frequency optic phonon modes (≤ 30 cm^{-1}), the main contribution comes from the vibrations of the Ag-Te cluster in the $AgGaTe_2$ and $AgInTe_2$ compounds, and the vibrations of Te atoms in the $CuGaTe_2$ and $CuInTe_2$ compounds. Cluster vibrations can substantially scatter the heat-carrying phonons and thus lower the thermal conductivity.[9] All the above considerations lead to the smaller thermal conductivities observed in the $AgGaTe_2$ and $AgInTe_2$ compounds compared to the $CuGaTe_2$ and $CuInTe_2$ structures.

To validate the calculated phonon dispersion relations, the experimental heat capacity was compared with the theoretically calculated heat capacity for each sample obtained with the aid of calculated phonon dispersion relations. According to the theory for the specific heat of solids, the heat capacity is obtained from Eq. 8:[83]

$$C_{\mathrm{V}} = \left(\frac{\partial \bar{E}}{\partial T}\right)_V = \int_0^{\omega_m} k_B \left(\frac{\hbar\omega}{k_B T}\right)^2 \frac{e^{\hbar\omega/k_B T} g(\omega)\, d\omega}{(e^{\hbar\omega/k_B T} - 1)^2}. \quad (8)$$

Here, $g(\omega)$ is the phonon density of states, and ω_m represents the maximum frequency in the phonon spectrum that satisfies the following criterion: $\int_0^{\omega_m} g(\omega)\, d\omega = 3N$, where N is the number of atoms per formula unit. As shown in **Figure 8c**, the boson peak is observed in the theoretical curve of the temperature dependent reduced heat capacity (C_p/T^3), and the variation trend is semi-quantitatively consistent with the experimental results shown in

This article is protected by copyright. All rights reserved.

Author Manuscript

Figure 8b. The results corroborate that coupling between acoustic phonons and low-frequency optical phonons induces the boson peak in all four compounds. Moreover, the difference in the coupling content among the four compounds contributes to their distinct avoided-crossing frequencies, sound velocities, and thermal conductivities.

Apart from the intrinsic characteristics of lattice vibrations discussed above, the thermal conductivity is also closely related to the predominant phonon scattering mechanism acting at different temperatures. To evaluate the strength of each phonon scattering mechanism in these four compounds, we have measured the low temperature thermal conductivities (**Figure 10a**), and have fitted the data using the Debye-Callaway model:[84,85]

$$\kappa_L = \frac{k_B}{2\pi^2 v}\left(\frac{k_B}{\hbar}\right)^3 T^3 \int_0^{\frac{\theta_D}{T}} \frac{x^4 e^x}{\tau_c^{-1}(e^x-1)^2} dx. \quad (9)$$

Here, x is defined as $x = \hbar\omega/k_B T$, and τ_c represents the overall relaxation time. In this study, Umklapp scattering, grain boundary scattering, point defect scattering, and phonon resonance scattering are included. Taking these processes as substantially independent, the relaxation rate is:[81,86,87]

$$\begin{aligned}\tau_c^{-1} &= \tau_B^{-1} + \tau_D^{-1} + \tau_U^{-1} + \tau_R^{-1} \\ &= \frac{v}{L} + A\omega^4 + B\omega^2 T e^{-\frac{\theta_D}{3T}} + \left[\frac{C_1\omega^2}{(\omega_1^2-\omega^2)^2} + \frac{C_2\omega^2}{(\omega_1^2-\omega^2)^2}\right]. \quad (10)\end{aligned}$$

In the above equation, τ_B, τ_D, τ_U and τ_R represent the relaxation time for grain boundary scattering, point defect scattering, Umklapp scattering, and phonon resonance scattering, respectively. And L is the average grain size in the samples, and constants A and B are the

This article is protected by copyright. All rights reserved.

Author Manuscript

fitting parameters for point defect scattering and Umklapp scattering, respectively. In the fourth term in Eq. 10, C_1 and C_2 are constants proportional to the concentration of the oscillators, and ω_1 and ω_2 are the frequencies obtained from fitting the heat capacity. The resulting parameters are presented in **Table 4**. The fraction that each scattering process contributes to the thermal transport, as well as differences among the four samples, can be derived from these parameters. At extremely low temperatures (T<15 K), grain boundary scattering and point defect scattering dominate the thermal transport process. Hence, the lattice thermal conductivities of the four compounds show little difference with the larger L values in the $AgGaTe_2$ and $AgInTe_2$ samples but the smaller A values in the $CuGaTe_2$ and $CuInTe_2$ samples. As temperature further increases, the Umklapp scattering starts to account for a greater fraction of the lattice thermal conductivity, the larger B parameter values result in lower lattice thermal conductivity of the $AgGaTe_2$ and $AgInTe_2$ compounds. Thus, the different strengths of various scattering processes are also an important factor in understanding the different thermal transport properties of the four compounds. We estimated the phonon mean free path based on a kinetic formulation of the thermal conductivity, $\kappa_{\mathrm{L}} = 1/3\, Cvl$. The dramatically reduced phonon mean free path in the $AgGaTe_2$ and $AgInTe_2$ compounds depicted in **Figure 10b** further indicates that the propagation of phonons is more strongly impeded in $AgGaTe_2$ and $AgInTe_2$ compounds than in $CuGaTe_2$ and $CuInTe_2$ compounds. Moreover, The Ag-containing compounds show a much sharper decrease below 50 K in their phonon mean free path, indicating stronger coupling between the acoustical phonons and low-frequency optical phonons.

3. Conclusions

This article is protected by copyright. All rights reserved.

Author Manuscript

In this work, the electrical and thermal transport properties of four pristine chalcopyrite compounds $ABTe_2$ (A=Cu, Ag; B=Ga, In) with promising thermoelectric performance are discussed. The underlying mechanism for the distinction of electrical and thermal transport properties among these four compounds with similar crystal chemistry mainly originates from the differences in the character of chemical bonds, the positions of deep-level states, phonon dispersion, and anharmonicity, etc. Owing to the ionization process of impurity bands with different ionization energies, different characteristic temperatures of intrinsic semiconductor to degenerate semiconductor transitions and different electrical transport properties are observed. Concerning thermal transport properties, based on the calculated phonon dispersion and compared with $CuGaTe_2$ and $CuInTe_2$ samples, $AgGaTe_2$ and $AgInTe_2$ with the vibrations of Ag-Te clusters possess lower avoided-crossing frequencies and smaller slopes in acoustic phonon dispersions, resulting in lower thermal conductivities and sound velocity in thermal transport properties. Moreover, the calculated phonon dispersion relations reveal that the coupling between acoustic phonons and low-frequency optic phonons plays an important role in the presence of the Boson peaks. The discrepancy of thermal conductivity among these four compounds is related to the degree of coupling between the acoustical phonons and low-frequency optical phonons. All the above factors contribute to the highest electrical conductivity of 2.82×10^{3} S/m and thermal conductivity of 7.26 $Wm^{-1}K^{-1}$ at 300 K in $CuGaTe_2$, while $AgInTe_2$ sample possesses the lowest electrical conductivity of 1.71×10^{-2} S/m and thermal conductivity of 1.47 $Wm^{-1}K^{-1}$ at 300 K.

Author Manuscript

This article is protected by copyright. All rights reserved.

4. Experimental Section

Synthesis: High-purity Ag (shot, 99.99%, Sinopharm Chemical Reagent Co., Ltd®), Cu (shot, 99.99%, Sinopharm Chemical Reagent Co., Ltd®), Ga (shot, 99.99%, Sinopharm Chemical Reagent Co., Ltd®), In (shot, 99.99%, Sinopharm Chemical Reagent Co., Ltd®) and Te (shot, 99.999%, Sinopharm Chemical Reagent Co., Ltd®) were weighed and mixed according to the stoichiometric composition of $ABTe_2$ (A=Cu, Ag; B=Ga, In). The mixtures were loaded into evacuated quartz tubes with the inner diameter of 16 mm, and were heated slowly with the heating rate of 100 K/h to 1273 K, dwelt for 24 h. The quartz tubes were then quenched in supersaturated salt water. Subsequently, the quenched samples were annealed for 24 h at 823 K. The as-obtained ingots were ground into fine powders, which were sintered with the assistance of a spark plasma sintering (SPS) apparatus at 773 K under 45 MPa to obtain fully-densified bulk cylindrical samples ($\phi 16\times3.5$ mm^3) with a relative density above 98%. The obtained bulks were then cut into proper sizes for structural and transport characterization.

Structure characterization & microstructure: The phase composition of the samples was examined by powder X-ray diffraction analysis (XRD; Empyrean, PANalytical®; Cu Kα). The working voltage of the electron gun is 40 kV, and the measuring step size is 0.0033 º with a collecting range from 5 º to 140 º to obtain the lattice constants. The morphology of the samples was investigated using field-emission scanning electron microscopy (FESEM, Hitachi ®SU-8020, Japan).

Author Manuscript

This article is protected by copyright. All rights reserved.

Thermoelectric properties measurement: The electrical conductivity and the Seebeck coefficient from 300 K to 873 K were measured under the atmosphere of helium gas by a standard four-probe method (ZEM-3, Ulvac-Riko®, Japan). The thermal conductivity was calculated according to the formula $\kappa = DC_{\mathrm{p}}\rho$, where D is the thermal diffusivity measured under the atmosphere of argon gas via a laser flash system (LFA-457, Netzsch®, Germany), C_{p} is the heat capacity calculated by the Dulong-Petit law, and ρ is the density measured by the method of Archimedes. The electrical conductivity, Seebeck coefficient, thermal conductivity, heat capacity, and Hall coefficient at low temperatures were measured by a Physical Property Measurement System (PPMS, Quantum Design®, San Diego, CA, USA). The carrier concentration and Hall mobility from 300 K to 673 K were measured by a home-made apparatus[88] in the field of 1 Tesla. The carrier concentration (n) and hall mobility (μ) were calculated according to the following formulas $n = 1/(eR_{\mathrm{H}})$ and $\mu = \sigma R_{\mathrm{H}}$, where e is the electron charge, R_{H} is the hall coefficient, and σ is the electrical conductivity.

Spectral characterization: The absorption coefficient of the samples from 200 nm to 2500 nm was measure by a Shimadzu® UV-3600 PC double-beam, double-monochromator spectrophotometer. Fourier-transformed infrared spectra from 400 to 4000 cm^{-1} were collected on a Nicolet® 6700 IR spectrometer. The working function was measured using UPS (VG® Multilab 2000) with samples of standard silver used for calibration.

Author Manuscript

This article is protected by copyright. All rights reserved.

Calculations of phonon dispersion relations: First-principles calculations based on the density functional theory (DFT) were carried out using Quantum Espresso[89] software. Norm-conserving scalar relativistic pseudo-potentials along with the PBE functional under general gradient approximation (GGA)[90] were employed. For geometrical structure relaxation, a Monkhorst-pack[91] 12× 12 × 6 *k*-grid and a cut-off energy of 78 Ry were adopted. The structures were considered as fully relaxed, including the lattice constants and atomic positions, when the energy and force converged to within 10^{-6} Ry and 10^{-5} Ry/Bohr, respectively. With the relaxed structure, density functional perturbation theory (DFPT) was used to calculate the second-order inter-atomic force constant with a 4 × 4 × 4 *q*-grid, and therein the phonon dispersion relation and phonon density of states. To obtain the phonon density of states, a find gird of 45 × 45 × 45 was used for sampling the first Brillouin zone.

Acknowledgements

The authors from the WUT wish to acknowledge support from the National Key Research and Development Program of China (Grant No. 2019YFA0704900), the Natural Science Foundation of China (51972256, 51872219, 51632006, and 51521001), the 111 Project of China (Grant No. B07040), and the Fundamental Research Funds for the Central Universities (WUT: 2020IVB056). The research of TPB and CU is supported by a Grant No. DE-SC0018941 from the U.S. Department of Energy.

Author Manuscript

This article is protected by copyright. All rights reserved.

References

[1] G. Tan, L. D. Zhao, M. G. Kanatzidis, *Chem. Rev.* **2016**, *116*, 12123.

[2] K. Biswas, J. He, I. D. Blum, C.-I. Wu, T. P. Hogan, D. N. Seidman, V. P. Dravid, M. G. Kanatzidis, *Nature* **2012**, *489*, 414.

[3] Z. L. Wang, W. Wu, *Angew. Chem. Int. Ed.* **2012**, *51*, 11700.

[4] S. Ortega, M. Ibáñez, Y. Liu, Y. Zhang, M. V. Kovalenko, D. Cadavid, A. Cabot, *Chem. Soc. Rev.* **2017**, *46*, 3510.

[5] X. Su, P. Wei, H. Li, W. Liu, Y. Yan, P. Li, C. Su, C. Xie, W. Zhao, P. Zhai, Q. Zhang, X. Tang, C. Uher, *Adv. Mater.* **2017**, *29*, 1602013.

[6] W. Liu, J. Hu, S. Zhang, M. Deng, C.-G. Han, Y. Liu, *Mater. Today Phys.* **2017**, *1*, 50.

[7] W. Liu, J. Zhou, Q. Jie, Y. Li, H. S. Kim, J. Bao, G. Chen, Z. Ren, *Energy Environ. Sci.* **2016**, *9*, 530.

[8] R. Deng, X. Su, S. Hao, Z. Zheng, M. Zhang, H. Xie, W. Liu, Y. Yan, C. Wolverton, C. Uher, M. G. Kanatzidis, X. Tang, *Energy Environ. Sci.* **2018**, *11*, 1520.

[9] Y. Li, Z. Li, C. Zhang, D. Yang, T. Liu, Y. Yan, W. Liu, G. Tan, X. Su, C. Uher, X. Tang, *Mater. Today Phys.* **2019**, *9*, 100098.

[10] G. J. Snyder, A. H. Snyder, *Energy Environ. Sci.* **2017**, *10*, 2280.

[11] J. He, T. M. Tritt, *Science* **2017**, *357*, eaak9997.

[12] P. Ying, X. Li, Y. Wang, J. Yang, C. Fu, W. Zhang, X. Zhao, T. Zhu, *Adv. Funct. Mater.* **2017**, *27*, 1604145.

[13] X. Su, S. Hao, T. P. Bailey, S. Wang, I. Hadar, G. Tan, T.-B. Song, Q. Zhang, C. Uher, C. Wolverton, X. Tang, M. G. Kanatzidis, *Adv. Energy Mater.* **2018**, *8*, 1800659.

[14] W. G. Zeier, A. Zevalkink, Z. M. Gibbs, G. Hautier, M. G. Kanatzidis, G. J. Snyder, *Angew. Chem. Int. Ed.* **2016**, *55*, 6826.

[15] Q. Zhang, E. K. Chere, J. Sun, F. Cao, K. Dahal, S. Chen, G. Chen, Z. Ren, *Adv. Energy Mater.* **2015**, *5*, 1500360.

Author Manuscript

This article is protected by copyright. All rights reserved.

[16] S. Anand, K. Xia, T. Zhu, C. Wolverton, G. J. Snyder, *Adv. Energy Mater.* **2018**, *8*, 1801409.

[17] G. Tan, F. Shi, S. Hao, H. Chi, L. D. Zhao, C. Uher, C. Wolverton, V. P. Dravid, M. G. Kanatzidis, *J. Am. Chem. Soc.* **2015**, *137*, 5100.

[18] Y. Xiao, H. Wu, W. Li, M. Yin, Y. Pei, Y. Zhang, L. Fu, Y. Chen, S. J. Pennycook, L. Huang, J. He, L.-D. Zhao, *J. Am. Chem. Soc.* **2017**, *139*, 18732.

[19] K. Ahn, H. Shin, J. Im, S. H. Park, I. Chung, *ACS Appl. Mater. Interfaces* **2017**, *9*, 3766.

[20] W. Li, L. Zheng, B. Ge, S. Lin, X. Zhang, Z. Chen, Y. Chang, Y. Pei, *Adv. Mater.* **2017**, *29*, 1605887.

[21] G. Zheng, X. Su, H. Xie, Y. Shu, T. Liang, X. She, W. Liu, Y. Yan, Q. Zhang, C. Uher, M. G. Kanatzidis, X. Tang, *Energy Environ. Sci.* **2017**, *10*, 2638.

[22] Y. Li, X. Wang, G. Liu, B. Shin, F. Shan, *Scripta Mater.* **2019**, *172*, 88.

[23] G. Zheng, X. Su, X. Li, T. Liang, H. Xie, X. She, Y. Yan, C. Uher, M. G. Kanatzidis, X. Tang, *Adv. Energy Mater.* **2016**, *6*, 1600595.

[24] Y. Tang, R. Hanus, S. Chen, G. J. Snyder, *Nat. Commun.* **2015**, *6*, 1.

[25] A. Moure, M. Rull-Bravo, B. Abad, A. Del Campo, M. M. Rojo, M. H. Aguirre, A. Jacquot, J. F. Fernandez, M. Martin-Gonzalez, *Nano Energy* **2017**, *31*, 393.

[26] P. Zong, R. Hanus, M. Dylla, Y. Tang, J. Liao, Q. Zhang, G. J. Snyder, L. Chen, *Energy Environ. Sci.* **2017**, *10*, 183.

[27] G. Tan, F. Shi, S. Hao, H. Chi, T. P. Bailey, L. D. Zhao, C. Uher, C. Wolverton, V. P. Dravid, M. G. Kanatzidis, *J. Am. Chem. Soc.* **2015**, *137*, 11507.

[28] G. Tan, S. Hao, R. C. Hanus, X. Zhang, S. Anand, T. P. Bailey, A. J. E. Rettie, X. Su, C. Uher, V. P. Dravid, G. J. Snyder, C. Wolverton, M. G. Kanatzidis, *ACS Energy Lett.* **2018**, *3*, 705.

[29] A. Banik, U. S. Shenoy, S. Saha, U. V. Waghmare, K. Biswas, *J. Am. Chem. Soc.* **2016**, *138*, 13068.

[30] Y.-L. Pei, J. He, J.-F. Li, F. Li, Q. Liu, W. Pan, C. Barreteau, D. Berardan, N. Dragoe, L.-D. Zhao, *NPG Asia Mater.* **2013**, *5*, e47.

Author Manuscript

This article is protected by copyright. All rights reserved.

[31] L.-D. Zhao, J. He, D. Berardan, Y. Lin, J.-F. Li, C.-W. Nan, N. Dragoe, *Energy Environ. Sci.* **2014**, *7*, 2900.

[32] D. Yang, X. Su, Y. Yan, T. Hu, H. Xie, J. He, C. Uher, M. G. Kanatzidis, X. Tang, *Chem. Mater.* **2016**, 13.

[33] X. Su, N. Zhao, S. Hao, C. C. Stoumpos, M. Liu, H. Chen, H. Xie, Q. Zhang, C. Wolverton, X. Tang, M. G. Kanatzidis, *Adv. Funct. Mater.* **2019**, *29*, 1806534.

[34] D. Parker, D. J. Singh, *Phys. Rev. B* **2012**, *85*, 125209.

[35] X. Cheng, Y. You, J. Fu, T. Hu, W. Liu, X. Su, Y. Yan, X. Tang, *J. Alloy. Compd.* **2018**, *750*, 965.

[36] Y. Li, G. Liu, T. Cao, L. Liu, J. Li, K. Chen, L. Li, Y. Han, M. Zhou, *Adv. Funct. Mater.* **2016**, *26*, 6025.

[37] L. Xi, Y. B. Zhang, X. Y. Shi, J. Yang, X. Shi, L. D. Chen, W. Zhang, J. Yang, D. J. Singh, *Phys. Rev. B* **2012**, *86*, 155201.

[38] Q. Tan, W. Sun, Z. Li, J.-F. Li, *J. Alloy. Compd.* **2016**, *672*, 558.

[39] H. Xie, X. Su, G. Zheng, T. Zhu, K. Yin, Y. Yan, C. Uher, M. G. Kanatzidis, X. Tang, *Adv. Energy Mater.* **2016**, *7*, 1601299.

[40] H. Takaki, K. Kobayashi, M. Shimono, N. Kobayashi, K. Hirose, N. Tsujii, T. Mori, *Mater. Today Phys.* **2017**, *3*, 85.

[41] S. W. Lovesey, K. S. Knight, C. Detlefs, S. W. Huang, V. Scagnoli, U. Staub, *J. Phys.: Cond. Mat.* **2012**, *24*, 216001.

[42] L. Xue, B. Xu, D. Zhao, L. Yi, *Intermetallics* **2014**, *55*, 204.

[43] Y. Zhong, P. Wang, H. Mei, Z. Jia, N. Cheng, *Semicond. Sci. Technol.* **2018**, *33*, 065014.

[44] J. Shen, X. Zhang, Z. Chen, S. Lin, J. Li, W. Li, S. Li, Y. Chen, Y. Pei, *J. Mater. Chem. A* **2017**, *5*, 5314.

[45] W. D. Carr, D. T. Morelli, *J. Alloy. Compd.* **2015**, *630*, 277.

[46] T. Plirdpring, K. Kurosaki, A. Kosuga, T. Day, S. Firdosy, V. Ravi, G. J. Snyder, A. Harnwunggmoung, T. Sugahara, Y. Ohishi, H. Muta, S. Yamanaka, *Adv. Mater.* **2012**, *24*, 3622.

Author Manuscript

This article is protected by copyright. All rights reserved.

[47] Z. Xia, G. Wang, X. Zhou, W. Wen, *Mater. Res. Bull.* **2018**, *101*, 184.

[48] R. Liu, Y. Qin, N. Cheng, J. Zhang, X. Shi, Y. Grin, L. Chen, *Inorg. Chem. Front.* **2016**, *3*, 1167.

[49] R. Liu, L. Xi, H. Liu, X. Shi, W. Zhang, L. Chen, *Chem. Commun.* **2012**, *48*, 3818.

[50] Y. Zhong, Y. Luo, X. Li, J. Cui, *Sci. Rep.* **2019**, *9*, 18879.

[51] A. Yusufu, K. Kurosaki, A. Kosuga, T. Sugahara, Y. Ohishi, H. Muta, S. Yamanaka, *Appl. Phys. Lett.* **2011**, *99*, 061902.

[52] R. Funahashi, S. Urata, K. Mizuno, T. Kouuchi, M. Mikami, *Appl. Phys. Lett.* **2004**, *85*, 1036.

[53] J. Androulakis, I. Todorov, D.-Y. Chung, S. Ballikaya, G. Wang, C. Uher, M. Kanatzidis, *Phys. Rev. B* **2010**, *82*, 115209.

[54] Y.-J. Kim, L.-D. Zhao, M. G. Kanatzidis, D. N. Seidman, *ACS Appl. Mater. Interfaces* **2017**, *9*, 21791.

[55] K. C. Mandal, A. Smirnov, U. N. Roy, A. Burger, *Mater. Res. Soc. Symp. Proc.* **2002**, *744*, 131.

[56] J. Shewchun, J. J. Loferski, R. Beaulieu, G. H. Chapman, B. K. Garside, *J. Appl. Phys.* **1979**, *50*, 6978.

[57] J. Krustok, A. Jagomagi, M. Grossberg, J. Raudoja, M. Danilson, *Solar Energy Mater. Sol. Cells* **2006**, *90*, 1973.

[58] J. Krustok, J. Raudoja, M. Yakushev, R. D. Pilkington, H. Collan, *J. Appl. Phys.* **1999**, *86*, 5305.

[59] A. Jagomägi, J. Krustok, J. Raudoja, M. Grossberg, I. Oja, M. Krunks, M. Danilson, *Thin Solid Films* **2005**, *480–481*, 246.

[60] Y. Pei, J. Lensch-Falk, E. S. Toberer, D. L. Medlin, G. J. Snyder, *Adv. Funct. Mater.* **2011**, *21*, 241.

[61] H. Wu, S. Chen, T. Ikeda, G. J. Snyder, *Acta Mater.* **2012**, *60*, 6144.

[62] B. K. Min, B. S. Kim, I. H. Kim, J. K. Lee, M. H. Kim, M. W. Oh, S. D. Park, H. W. Lee, *Electron. Mater. Lett.* **2011**, *7*, 255.

Author Manuscript

This article is protected by copyright. All rights reserved.

[63] B. Du, H. Li, J. Xu, X. Tang, C. Uher, *Chem. Mater.* **2010**, *22*, 5521.

[64] Y. Zhu, Y. Liu, M. Wood, N. Z. Koocher, Y. Liu, L. Liu, T. Hu, J. M. Rondinelli, J. Hong, G. J. Snyder, W. Xu, *Chem. Mater.* **2019**, *31*, 8182.

[65] D. Schmid, M. Ruckh, F. Grunwald, H. W. Schock, *J. Appl. Phys.* **1993**, *73*, 2902.

[66] A. Congiu, L. Garbato, P. Manca, *Mater. Res. Bull.* **1973**, *8*, 293.

[67] P.-W. Chiang, D. F. O'Kane, D. R. Mason, *J. Electrochem. Soc.* **1967**, *114*, 759.

[68] G. Tan, W. G. Zeier, F. Shi, P. Wang, G. J. Snyder, V. P. Dravid, M. G. Kanatzidis, *Chem. Mater.* **2015**, *27*, 7801.

[69] W.-S. Liu, Q. Zhang, Y. Lan, S. Chen, X. Yan, Q. Zhang, H. Wang, D. Wang, G. Chen, Z. Ren, *Adv. Energy Mater.* **2011**, *1*, 577.

[70] A. I. Chumakov, G. Monaco, A. Monaco, W. A. Crichton, A. Bosak, R. Rüffer, A. Meyer, F. Kargl, L. Comez, D. Fioretto, H. Giefers, S. Roitsch, G. Wortmann, M. H. Manghnani, A. Hushur, Q. Williams, J. Balogh, K. Parliński, P. Jochym, P. Piekarz, *Phys. Rev. Lett.* **2011**, *106*, 225501.

[71] V. Lubchenko, P. G. Wolynes, *Proc. Natl. Acad. Sci. U.S.A.* **2003**, *100*, 1515.

[72] T. S. Grigera, V. Martín-Mayor, G. Parisi, P. Verrocchio, *Nature* **2003**, *422*, 289.

[73] E. Duval, A. Boukenter, T. Achibat, *J. Phys.: Cond. Mat.* **1990**, *2*, 10227.

[74] D. A. Parshin, H. R. Schober, V. L. Gurevich, *Phys. Rev. B* **2007**, *76*, 064206.

[75] H. Tanaka, *J. Phys. Soc. Japan* **2001**, *70*, 1178.

[76] A. I. Chumakov, I. Sergueev, U. van Bürck, W. Schirmacher, T. Asthalter, R. Rüffer, O. Leupold, W. Petry, *Phys. Rev. Lett.* **2004**, *92*, 245508.

[77] H. Shintani, H. Tanaka, *Nat. Mater.* **2008**, *7*, 870.

[78] J. He, D. Hitchcock, I. Bredeson, N. Hickman, T. M. Tritt, S. Zhang, *Phys. Rev. B* **2010**, *81*, 134302.

[79] V. Gurevich, D. Parshin, H. Schober, *Phys. Rev. B* **2003**, *67*, 094203.

[80] S. N. Taraskin, Y. L. Loh, G. Natarajan, S. R. Elliott, *Phys. Rev. Lett.* **2001**, *86*, 1255.

Author Manuscript

This article is protected by copyright. All rights reserved.

[81] H. Xie, X. Su, X. Zhang, S. Hao, T. P. Bailey, C. C. Stoumpos, A. P. Douvalis, X. Hu, C. Wolverton, V. P. Dravid, C. Uher, X. Tang, M. G. Kanatzidis, *J. Am. Chem. Soc.* **2019**, *141*, 10905.

[82] F. Liu, P. Parajuli, R. Rao, P. C. Wei, A. Karunarathne, S. Bhattacharya, R. Podila, J. He, B. Maruyama, G. Priyadarshan, J. R. Gladden, Y. Y. Chen, A. M. Rao, *Phys. Rev. B* **2018**, *98*, 224309.

[83] A. Fischer, E.-W. Scheidt, W. Scherer, D. E. Benson, Y. Wu, D. Eklöf, U. Häussermann, *Phys. Rev. B* **2015**, *91*, 224309.

[84] J. Callaway, *Phys. Rev.* **1959**, *113*, 1046.

[85] J. Callaway, H. C. von Baeyer, *Phys. Rev.* **1960**, *120*, 1149.

[86] J. Cohn, G. Nolas, V. Fessatidis, T. Metcalf, G. Slack, *Phys. Rev. Lett.* **1999**, *82*, 779.

[87] J. Yang, G. P. Meisner, D. T. Morelli, C. Uher, *Phys. Rev. B* **2000**, *63*, 014410.

[88] W. Zhao, Z. Liu, P. Wei, Q. Zhang, W. Zhu, X. Su, X. Tang, J. Yang, Y. Liu, J. Shi, Y. Chao, S. Lin, Y. Pei, *Nature Nanotech.* **2017**, *12*, 55.

[89] P. Giannozzi, S. Baroni, N. Bonini, M. Calandra, R. Car, C. Cavazzoni, D. Ceresoli, G. L. Chiarotti, M. Cococcioni, I. Dabo, A. D. Corso, S. de Gironcoli, S. Fabris, G. Fratesi, R. Gebauer, U. Gerstmann, C. Gougoussis, A. Kokalj, M. Lazzeri, L. Martin-Samos, N. Marzari, F. Mauri, R. Mazzarello, S. Paolini, A. Pasquarello, L. Paulatto, C. Sbraccia, S. Scandolo, G. Sclauzero, A. P. Seitsonen, A. Smogunov, P. Umari, R. M. Wentzcovitch, *J. Phys.: Cond. Mat.* **2009**, *21*, 395502.

[90] J. P. Perdew, K. Burke, M. Ernzerhof, *Phys. Rev. Lett.* **1996**, *77*, 3865.

[91] H. J. Monkhorst, J. D. Pack, *Phys. Rev. B* **1976**, *13*, 5188.

Author Manuscript

This article is protected by copyright. All rights reserved.

Author Manuscript

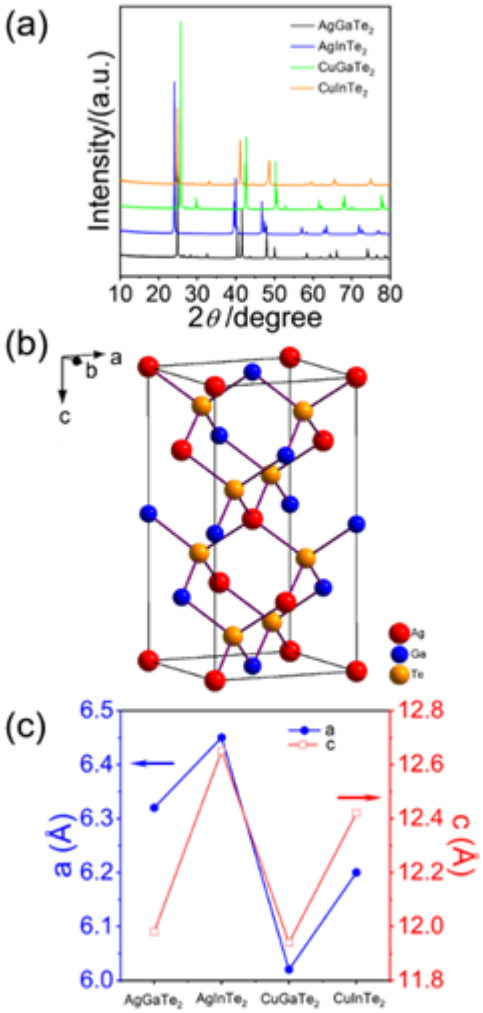

Figure 1. (a) Powder XRD patterns of $AgGaTe_2$, $AgInTe_2$, $CuGaTe_2$, and $CuInTe_2$, (b) crystal structure of $AgGaTe_2$ at room temperature, where the red spheres represent Ag or Cu atoms, the blue spheres represent Ga or In atoms, and the orange spheres represent Te atoms, and (c) the lattice parameters along the *a* and *c* axes of the four compounds.

This article is protected by copyright. All rights reserved.

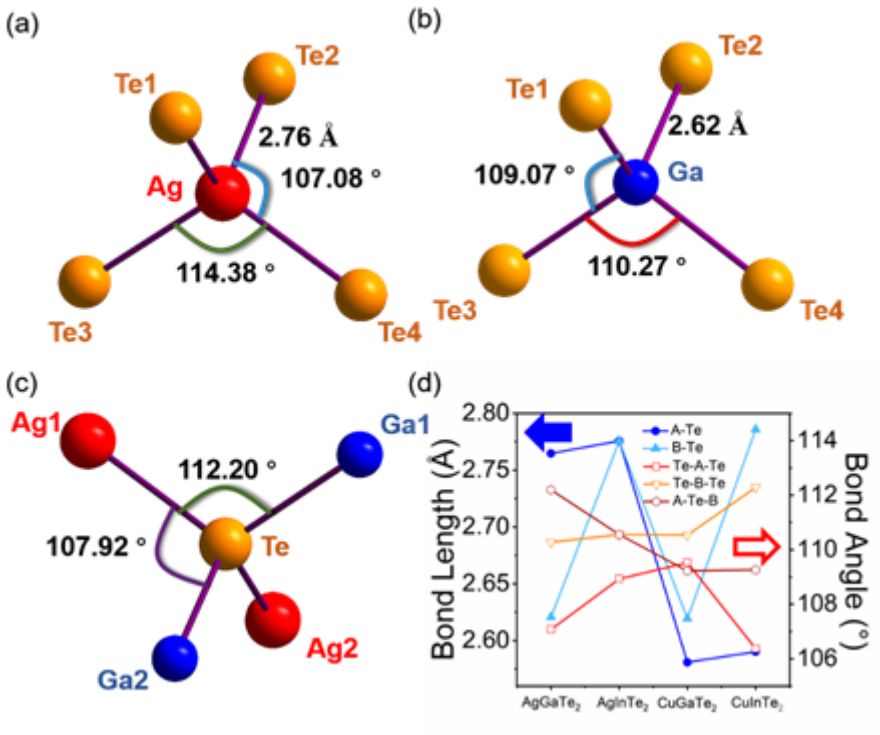

Figure 2. Coordinated environment of (a) Ag (center at the tetrahedral structure formed by four Te atoms), (b) Ga (center at the tetrahedral structure formed by four Te atoms), (c) Te (center at the tetrahedral structure formed by two Ag atoms and two Ga atoms), and (d) bond lengths and angles of the four compounds.

Author Manuscript

This article is protected by copyright. All rights reserved.

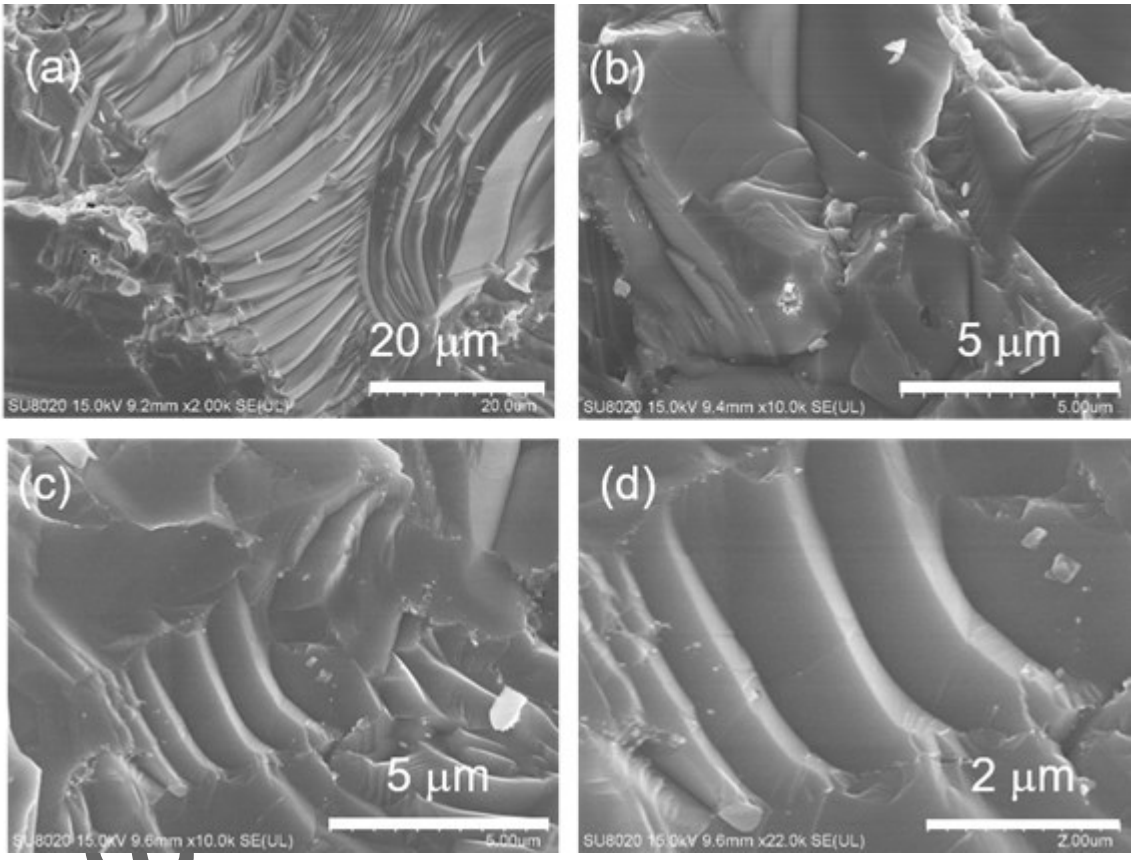

Figure 3. (a), (b), (c), and (d) Field emission scanning electron microscope images of fresh fracture surface in different areas of $CuGaTe_2$ bulk samples with different magnifications.

Author Ma

This article is protected by copyright. All rights reserved.

Author Manuscript

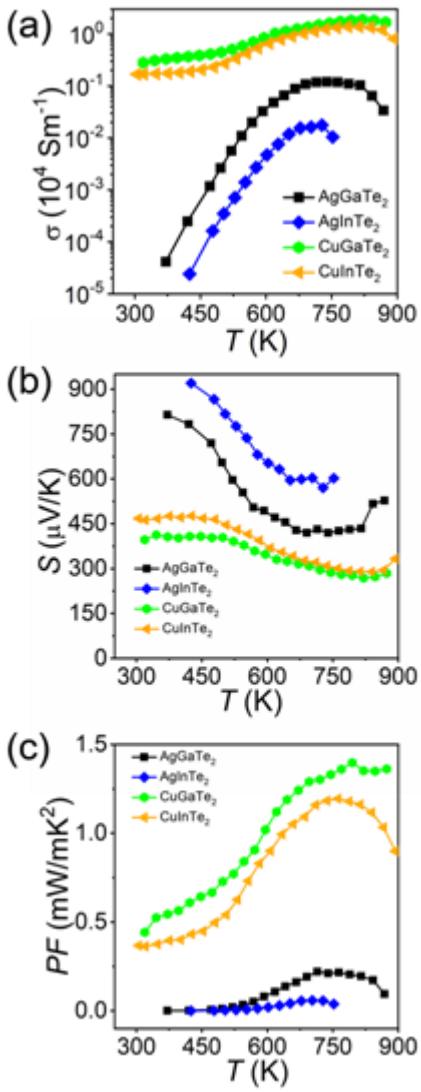

Figure 4. Temperature dependences of (a) the electrical conductivity, (b) Seebeck coefficient, and (c) power factor for $AgGaTe_2$, $AgInTe_2$, $CuGaTe_2$, and $CuInTe_2$.

This article is protected by copyright. All rights reserved.

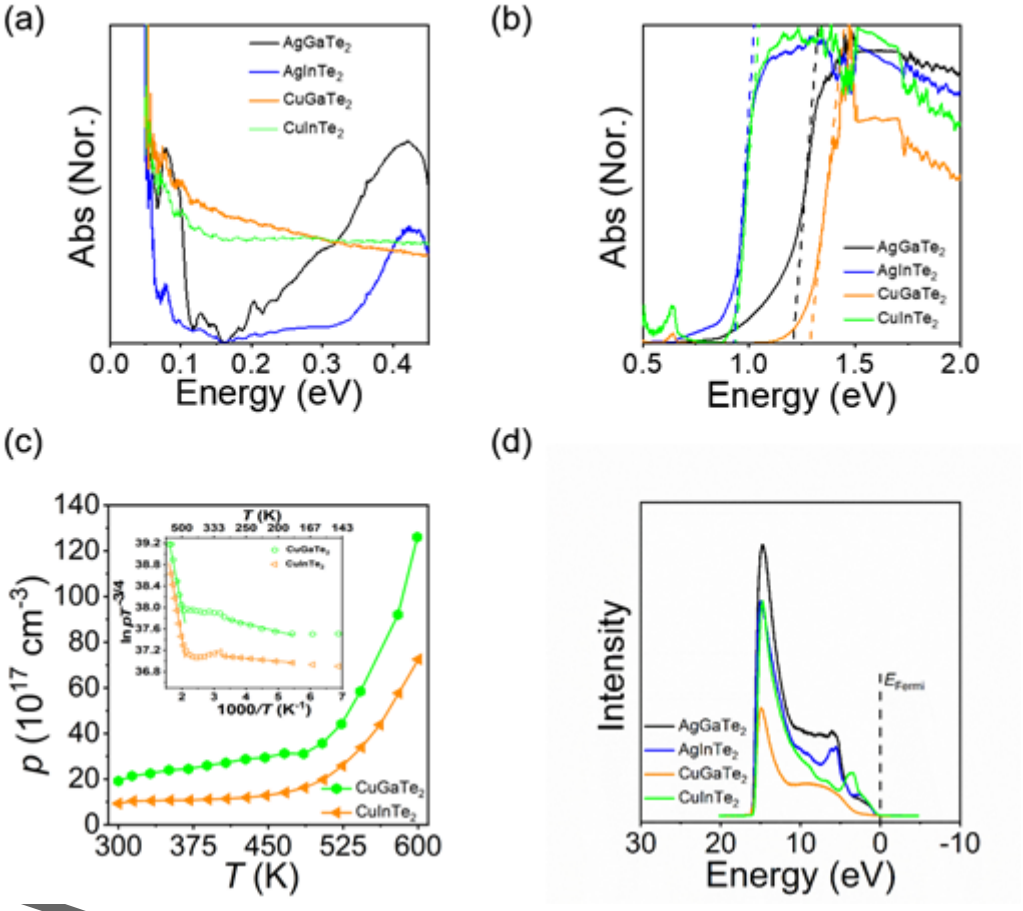

Figure 5. (a) Fourier-transformed infrared spectra and (b) UV-VIS absorption spectra for $AgGaTe_2$, $AgInTe_2$, $CuGaTe_2$, and $CuInTe_2$, (c) temperature dependences of carrier concentration for $CuGaTe_2$ and $CuInTe_2$ compounds, (d) ultraviolet photoelectron spectroscopy (UPS) for $AgGaTe_2$, $AgInTe_2$, $CuGaTe_2$, and $CuInTe_2$. The inset in c) plots $ln(pT^{-3/4})$ vs. $1000/T$ for $CuGaTe_2$ and $CuInTe_2$.

Author

This article is protected by copyright. All rights reserved.

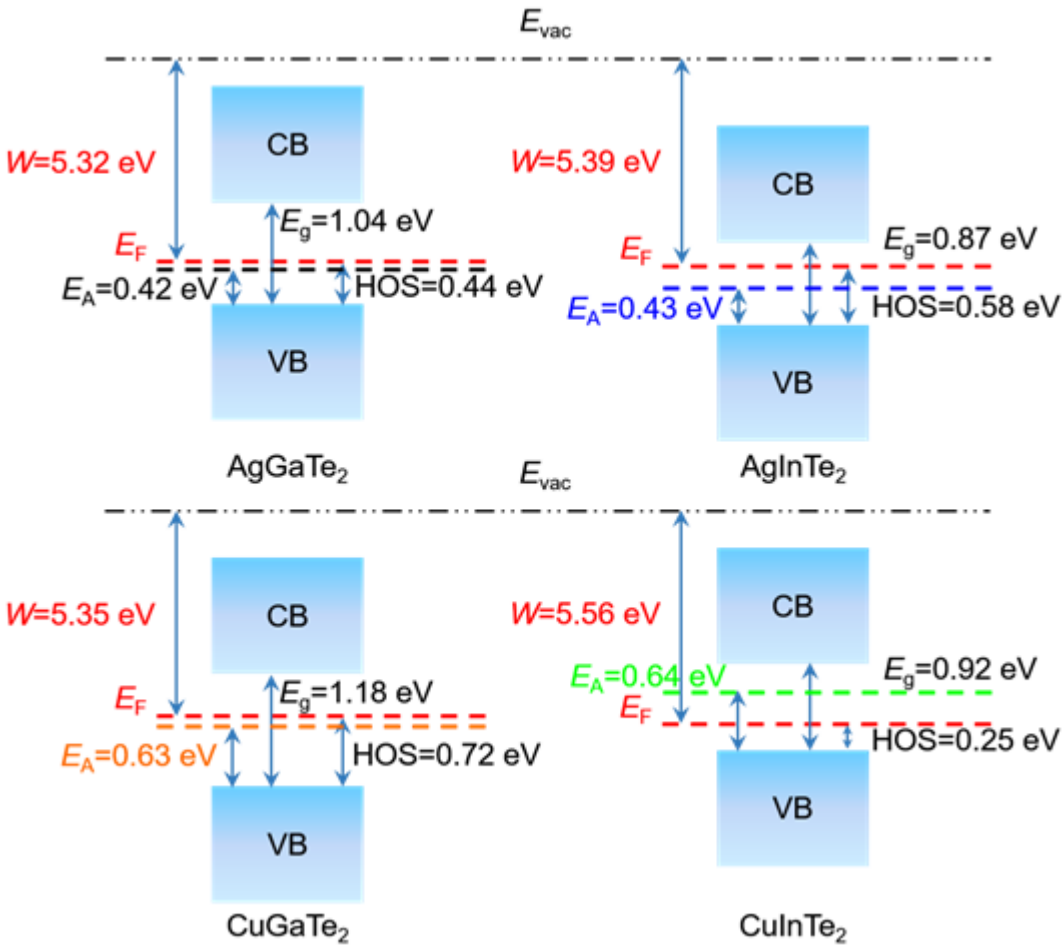

Figure 6. The electronic band structure diagrams of (a) $AgGaTe_2$, (b) $AgInTe_2$, (c) $CuGaTe_2$, and (d) $CuInTe_2$, where the W, E_F, E_A, E_g, and HOS represent the work function, Fermi level, ionization energy, band gap, and highest occupied state, respectively.

Author

This article is protected by copyright. All rights reserved.

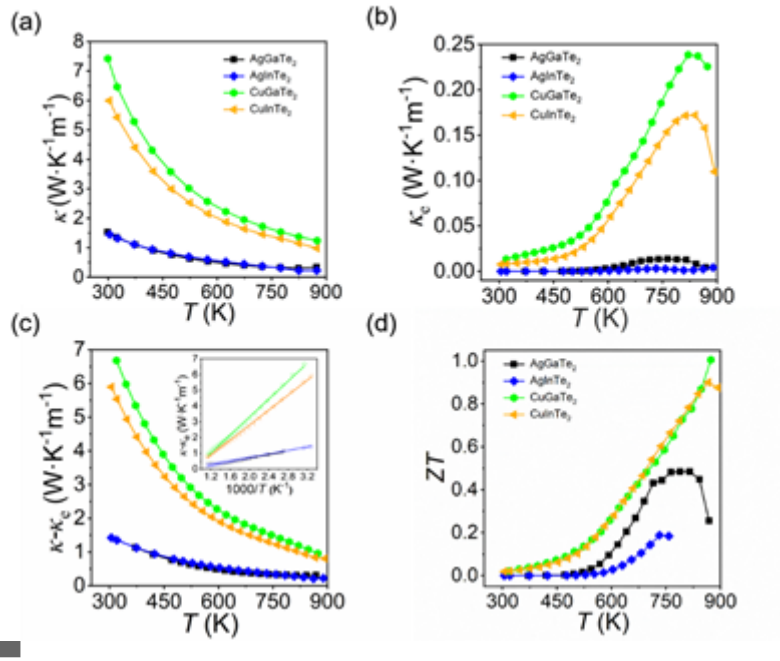

Figure 7. Temperature dependences of (a) the total thermal conductivity, (b) electronic thermal conductivity, (c) lattice thermal conductivity, and (d) *ZT* values for $AgGaTe_2$, $AgInTe_2$, $CuGaTe_2$, and $CuInTe_2$. The inset in c) plots the lattice thermal conductivity vs. 1000/*T* to show its inverse dependence on temperature.

Author Manuscript

This article is protected by copyright. All rights reserved.

Author Manuscript

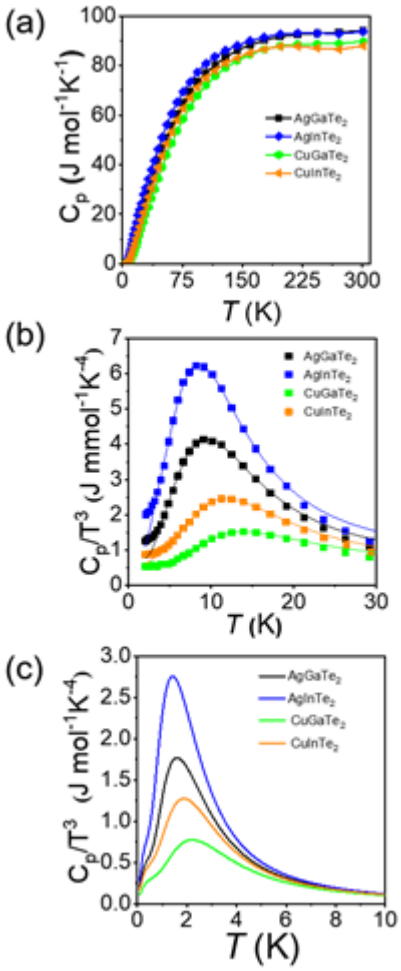

Figure 8. (a) Experimental specific heat data from 2 to 300 K, (b) the specific heat plotted as C_p/T^3 versus T, the solid lines are the fitting results of a Debye-Einstein model with two Einstein oscillators. The fitting parameters are presented in Table 2. (c) The calculated C_p/T^3 for $AgGaTe_2$, $AgInTe_2$, $CuGaTe_2$, and $CuInTe_2$.

This article is protected by copyright. All rights reserved.

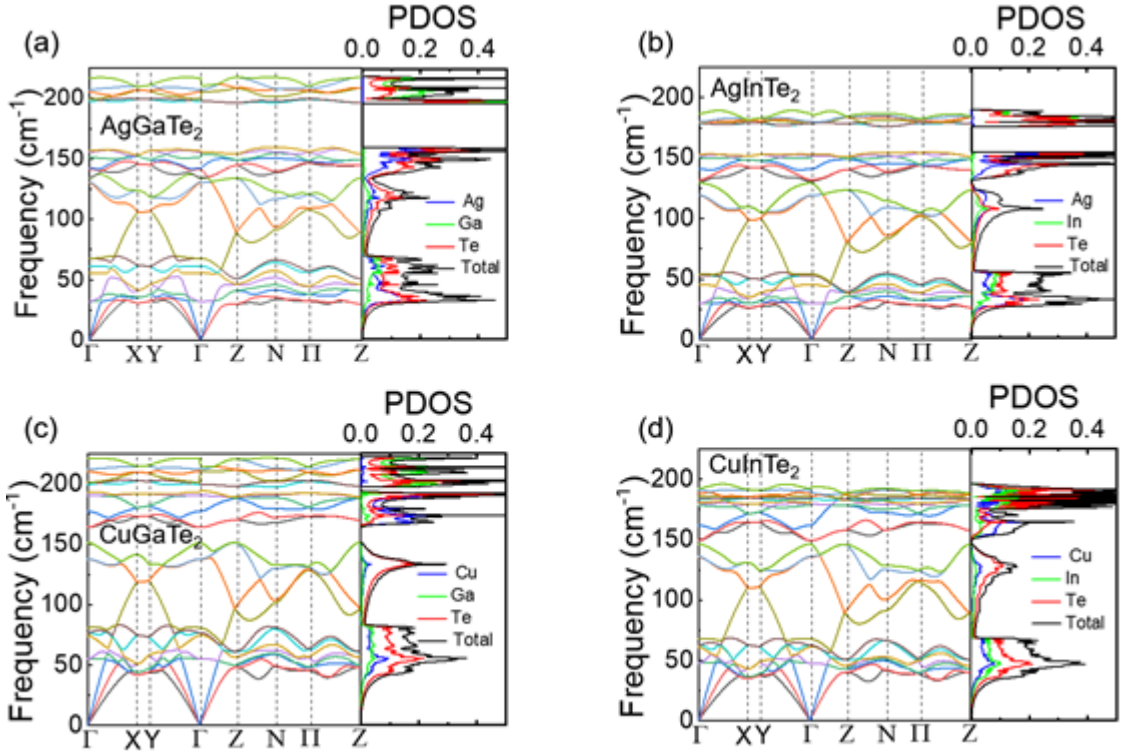

Figure 9. Calculated phonon dispersions and the corresponding phonon density of states of (a) $AgGaTe_2$, (b) $AgInTe_2$, (c) $CuGaTe_2$, and (d) $CuInTe_2$.

Author Ma

This article is protected by copyright. All rights reserved.

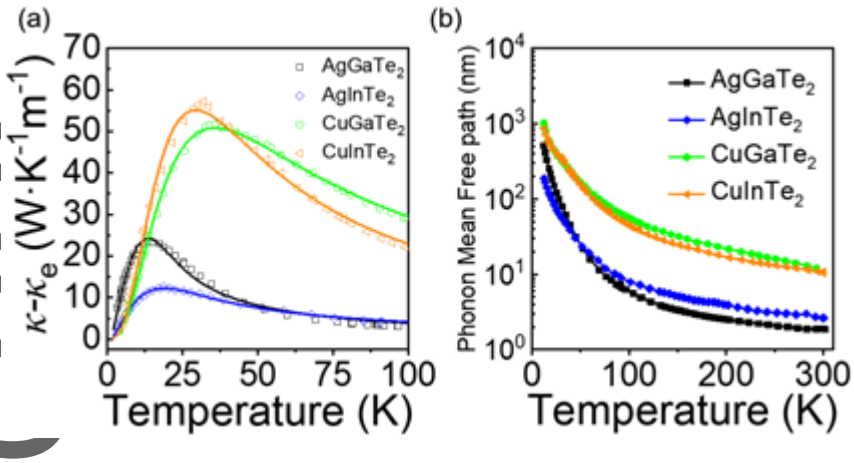

Figure 10. (a) Temperature dependent lattice thermal conductivities of $AgGaTe_2$, $AgInTe_2$, $CuGaTe_2$, and $CuInTe_2$. The solid lines are the calculated curves using the Debye-Callaway model. (b) Temperature dependences of the phonon mean free path in the four compounds.

Author Manuscript

This article is protected by copyright. All rights reserved.

Table 1. Crystal structure parameters including bond angles, bond lengths, and lattice parameters obtained from the structure refinement of the XRD data for $AgGaTe_2$, $AgInTe_2$, $CuGaTe_2$, and $CuInTe_2$.

Parameters		$AgGaTe_2$	$AgInTe_2$	$CuGaTe_2$	$CuInTe_2$
Bond Angles (*deg*)	**Te-A-Te (Ⅰ)**	107.1	108.9	109.5	106.4
	Te-A-Te (Ⅱ)	114.4	110.6	109.4	111.0
	Te-B-Te (Ⅰ)	109.1	108.9	108.9	108.1
	Te-B-Te (Ⅱ)	110.3	110.6	110.5	112.3
	A-Te-B (Ⅰ)	107.9	108.9	109.9	109.1
	A-Te-B (Ⅱ)	112.2	110.6	109.2	109.3
Bond Lengths (Å)	**A-Te**	2.76	2.78	2.58	2.59
	B-Te	2.62	2.78	2.62	2.78
lattice parameters (Å)	**a**	6.32	6.45	6.02	6.20
	b	6.32	6.45	6.02	6.20
	c	12.0	12.6	11.9	12.4

Author Manuscript

This article is protected by copyright. All rights reserved.

Table 2. The fitting parameters of the low-temperature heat capacity data of $AgGaTe_2$, $AgInTe_2$, $CuGaTe_2$, and $CuInTe_2$ by the Debye-Einstein model. Here, b is the Debye lattice term, A_i, and Θ_{Ei} are the amplitude and the Einstein temperature of the ith Einstein oscillator mode, and Θ_D is the Debye temperature.

Parameters	$AgGaTe_2$	$AgInTe_2$	$CuGaTe_2$	$CuInTe_2$
$\mathbf{b}$ $(\mathrm{mJ \cdot mol^{-1}K^{-4}})$	0.74	0.89	0.57	0.62
A_1	1.46	1.08	1.45	0.51
θ_{E1} (K)	28.4	22.8	49.9	27.8
A_2	17.4	19.8	13.7	17.7
θ_{E2} (K)	52.1	45.7	73.2	61.2
θ_D (K)	124	117	134	132

Author Manuscript

This article is protected by copyright. All rights reserved.

Table 3. The measured sound velocities (v_l, v_s, v_a) and the calculated elastic properties (E, G, v_p, γ and θ_D) of $AgGaTe_2$, $AgInTe_2$, $CuGaTe_2$, and $CuInTe_2$ at 300K.

Parameters	$AgGaTe_2$	$AgInTe_2$	$CuGaTe_2$	$CuInTe_2$
Shear sound velocity v_s(m/s)	1317	1378	2081	1817
Longitudinal sound velocity v_l(m/s)	2152	2252	3923	3592
Average sound velocity v_a(m/s)	1454	1521	2326	2037
Young's modulus E(GPa)	24.8	27.2	66.6	52.6
Shear modulus G(GPa)	10.3	11.3	25.5	19.8
Poisson ratio v_p	0.20	0.20	0.30	0.33
Grüeneissen parameter γ	1.29	1.29	1.80	1.96
Debye temperature θ_D(K)	139.9	143.3	230.7	195.7

Author Manuscript

This article is protected by copyright. All rights reserved.

Table 4. The fitting parameters of the low-temperature lattice thermal conductivity of $AgGaTe_2$ by the Debye-Callaway model. Here, L is the grain size, A and B are the constants for point defect scattering, and phonon-phonon scattering, C_1, and C_2 are the constants for phonon resonance scattering.

Compounds	L (μm)	A (10^{-41} s^3)	B (10^{-17} s/K)	C_1 (10^{33} s^{-3})	C_2 (10^{33} s^{-3})
$AgGaTe_2$	19.43	0.67	2.78	1.34	1.34
$AgInTe_2$	5.80	1.09	1.81	1.71	1.71
$CuGaTe_2$	3.23	0.04	0.22	1.71	1.71
$CuInTe_2$	2.85	0.03	0.40	1.71	1.71

Author Manuscript

This article is protected by copyright. All rights reserved.

Distinct electronic transport properties are observed among $ABTe_2$ (A=Cu, Ag; B=Ga, In) chalcopyrite compounds, resulting from the different physical characteristics of the deep-level in-gap states induced by the native A-site vacancies. Whereas the discrepancy in sound velocity, Grüeneissen parameter together with the coupling between the acoustic and low-frequency optical modes account for their different thermal transport properties.

Yu Cao[1], Xianli Su[1*], Fanchen Meng[2], Trevor P. Bailey[3], Jinggeng Zhao[4], Hongyao Xie[1], Jian He[2*], Ctirad Uher[3], Xinfeng Tang[1*]

Origin of the distinct thermoelectric transport properties of chalcopyrite $ABTe_2$ (A=Cu, Ag; B=Ga, In)

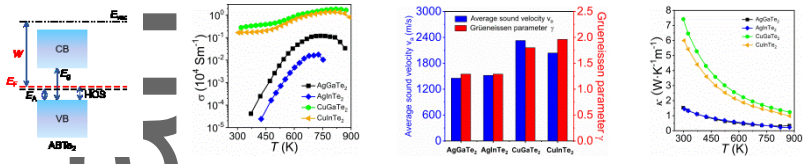

Author Manuscript

This article is protected by copyright. All rights reserved.